Ultrafast Science
A SCIENCE PARTNER JOURNAL

RESEARCH ARTICLE

Nonlocal Probing of Amplitude Mode Dynamics in Charge-Density-Wave Phase of $EuTe_4$

Ranjana Rathore[1,2*], Himanshu Singhal[1,2], Vivek Dwij[3,4], Mayanak K Gupta[2,5], Abhishek Pathak[3], Juzer Ali Chakera[1,2], Ranjan Mittal[2,5], Aditya Prasad Roy[3], Arun Babu[3], Ruta Kulkarni[4], A Thamizhavel[4], Ayman H Said[6], and Dipanshu Bansal[3,7,*]

[1]Laser Plasma Division, Raja Ramanna Centre for Advanced Technology, Indore, MP 452013, India. [2]Homi Bhabha National Institute, Training School Complex, Anushaktinagar, Mumbai, MH 400094, India. [3]Department of Mechanical Engineering, Indian Institute of Technology Bombay, Mumbai, MH 400076, India. [4]Department of Condensed Matter Physics & Materials Science, Tata Institute of Fundamental Research, Mumbai, MH 400005, India. [5]Solid State Physics Division, Bhabha Atomic Research Centre, Mumbai, MH 400085, India. [6]Advanced Photon Source, Argonne National Laboratory, 9700 South Cass Avenue, Lemont, IL 60439, USA. [7]Center for Research in Nano Technology and Science, Indian Institute of Technology Bombay, Mumbai, MH 400076, India.

*Address correspondence to: ranjana@rrcat.gov.in (R.R.); dipanshu@iitb.ac.in (D.B.)

Citation: Rathore R, Singhal H, Dwij V, Gupta MK, Pathak A, Chakera JA, Mittal R, Roy AP, Babu A, Kulkarni R, et al. Nonlocal Probing of Amplitude Mode Dynamics in Charge-Density-Wave Phase of $EuTe_4$. *Ultrafast Sci.* 2023;3:Article 0041. https://doi.org/10.34133/ultrafastscience.0041

Submitted 3 April 2023
Accepted 1 August 2023
Published 23 August 2023

Amplitude mode is collective excitation emerging from frozen lattice distortions below the charge-density-wave (CDW) transition temperature T_{CDW} and relates to the order parameter. Generally, the amplitude mode is non-polar (symmetry-even) and does not interact with incoming infrared photons. However, if the amplitude mode is polar (symmetry-odd), it can potentially couple with incoming photons, thus forming a coupled phonon–polariton quasiparticle that can travel with light-like speed beyond the optically excited region. Here, we present the amplitude mode dynamics far beyond the optically excited depth of ~150 nm in the CDW phase of ~10-μm-thick single-crystal $EuTe_4$ using time-resolved x-ray diffraction. The observed oscillations of the CDW peak, triggered by photoexcitation, occur at the amplitude mode frequency ω_{AM}. However, the underdamped oscillations and their propagation beyond the optically excited depth are at odds with the observation of the overdamped nature of the amplitude mode measured using meV-resolution inelastic x-ray scattering and polarized Raman scattering. The ω_{AM} is found to decrease with increasing fluence owing to a rise in the sample temperature, which is independently confirmed using polarized Raman scattering and ab-initio molecular dynamics simulations. We rationalize the above observations by explicitly calculating two coupled quasiparticles—phonon–polariton and exciton–polariton. Our data and simulations cannot conclusively confirm or rule out the one but point toward the likely origin from propagating phonon–polariton. The observed non-local behavior of amplitude mode thus provides an opportunity to engineer material properties at a substantially faster time scale with optical pulses.

Introduction

Charge-density-wave (CDW) order is a broken-symmetry state in metals that leads to a periodic spatial modulation of the charge-density at CDW wavevector $\mathbf{q}_{CDW}$ below the transition temperature T_{CDW} [1,2]. Several mechanisms, such as the Fermi surface nesting and hidden nesting [1–9], wavevector-dependent electron–phonon interaction [10–13], strong electron correlations [4,14,15], and a large electronic density of states at the Fermi level (E_F) in high-symmetry structures [16,17], are found to be the origin of CDW instability. The CDW instability is generally accompanied by lattice distortions, which are visible as Kohn anomalies above T_{CDW} [7–9,18]. The freezing of the CDW instability and lattice distortions below T_{CDW} at CDW wavevector $\mathbf{q}_{CDW}$ can be commensurate or incommensurate with the host lattice periodicity and leads to partial (only a few k-points) or full bandgap opening at E_F [19–30]. Below T_{CDW}, collective excitation emerges from the frozen lattice distortion and is referred to as the amplitude mode [31–38]. The amplitude mode relates to the CDW order parameter, and characterization of its dynamics is necessary to decipher the underlying mechanism of CDW instability.

The amplitude mode dynamics is typically probed using Raman scattering, inelastic x-ray scattering (IXS), time-resolved photoemission spectroscopy, and time-resolved x-ray/electron scattering, among others [12,13,19,31–34,36–41]. However, all the measurements as mentioned above generally measure local response within the optically excited volume, as the probe volume (from where the scattered radiation is collected) is the same or smaller. Recent pump-probe measurements have

shown that, under specific conditions, material properties are altered beyond the excited volume. Examples include ferroelectric polarization reversal in 50-μm-thick $LiNbO_3$ via phonon–polariton coupling [42], exciton–polariton coupling in InI single-crystals [43], and hybridization of phase mode exciton condensate and dispersion-less phonon mode in Ta_2NiSe_5 [44]. Here, in all examples, the origin of non-local behavior is owing to the generation of a new quasi-particle that propagates orders of magnitude faster through the materials than the speed of sound [42–46]. Hence, the observation of non-local behavior is of immense practical interest, as it highlights the opportunities to tailor material properties at substantially faster time scale (light-like speed for phonon–polariton and exciton–polariton) with external perturbations such as light.

The rare-earth tellurides ($R\mathrm{Te}_n$ for $n = 2$ to 4) are particularly interesting as they have readily accessible T_{CDW} and are actively being pursued to understand the amplitude mode dynamics [12,13,19,31,36,37,39,40]. Photoexcitation-induced coherent excitation of the amplitude mode; its overdamping and disappearance of CDW at higher fluence [19,31,37]; coupling of amplitude mode with phonons [36,39], electrons [12,13], or charge order [40]; enhancement of CDW amplitude on photoexcitation [41]; and amplitude mode exhibiting signatures of axial Higgs mode [47] highlight the complexity and intertwined nature of amplitude mode with other quasiparticle excitations in $R\mathrm{Te}_n$. Despite the above measurements with varying techniques, the coupling of amplitude mode with photon, enabling nonlocal behavior, is yet to be observed. The lack of observation stems from two reasons. The primary reason is the non-polar (symmetry-even) nature of the amplitude mode, which forbids the formation of the phonon–polariton quasiparticle [42,46]. The secondary reason is that the previous experimental setups were inherently designed to measure local response.

In this study, we focus on recently synthesized $EuTe_4$, an $n = 4$ family of $R\mathrm{Te}_n$ (see Fig. 1) [9,20,48], to observe amplitude mode–photon coupling enabled by the following favorable conditions. First, the amplitude mode in the non-centrosymmetric CDW phase of $EuTe_4$ is polar (symmetry-odd), which we explicitly confirm using group theory and symmetry analysis. The second is the high-quality growth of thin flakes (attenuation length is ~5 μm for 8.05 keV) that enables probe of non-local response using time-resolved x-ray diffraction (TXRD) measurements in the transmission geometry. Our TXRD measurements show oscillations far beyond the laser penetration depth. We rationalize the oscillation to originate from phonon–polariton propagation near the amplitude mode frequency ω_{AM}. The ω_{AM} value is consistent with our IXS measurements near $\mathbf{q}_{CDW}$. We find the oscillation frequency decreases on heating toward T_{CDW}, which is independently confirmed using temperature-dependent polarized Raman scattering measurements and ab-initio molecular dynamics (AIMD) simulations. Moreover, abundant electron–hole pairs at $\mathbf{q}_{CDW}$ lead to divergence of the electron–hole polarizability (Lindhard response function) in $EuTe_4$, which may excite the amplitude mode on photoexcitation. We also explore this possibility of exciton–polariton propagation for the observed oscillations.

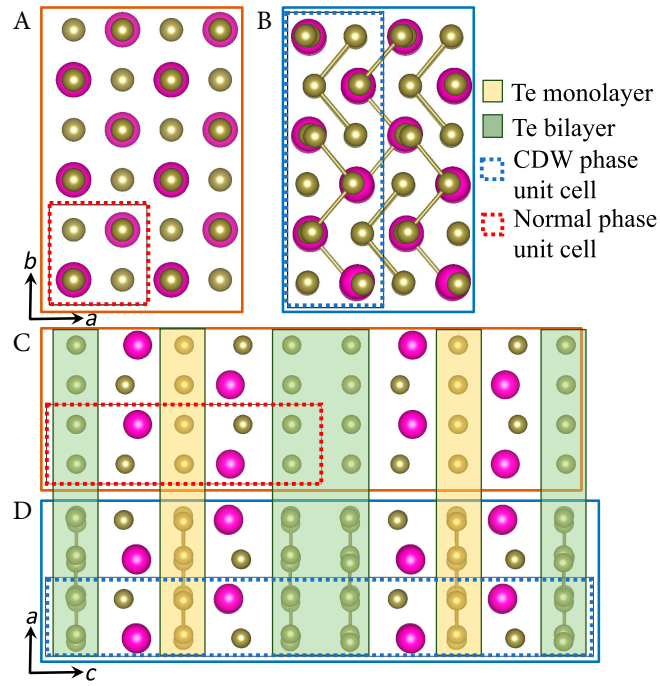

Fig. 1. Normal and CDW phase of $EuTe_4$. (A and B) Crystal structure of $EuTe_4$ in the normal phase in the *a*–*b* and *a*–*c* planes. Dashed red and blue rectangles mark unit cells of normal and CDW phases. Light yellow and green semi-transparent boxes highlight Te monolayer and bilayers. (C and D) Same as (A) and (B), but in the CDW phase. In the CDW phase, Te atoms form trimers in the monolayer and bilayer, as shown in both panels.

Methods

Time-resolved x-ray diffraction

Figure 3A shows the schematic of the TXRD experimental setup. TXRD experiments were carried out with an 800 nm (1.55 eV), 50 fs, ~5.7 mJ energy, laser pulse at a 1 kHz repetition rate. [49] The 10:90 (R:T) beam splitter splits the laser beam into two parts. The reflected beam passes through mirrors M2 to M4 and is focused on the sample using a plano-convex lens for photoexcitation. The transmitted beam is focused on a moving Cu wire (~350 μm diameter) target using an f/8 off-axis parabolic mirror (OAPM, focal spot 13.5 μm × 8.2 μm full width at half maximum [FWHM]) to generate the x-ray probe at 8.05 keV. A polycapillary lens focuses the x-rays on the sample (spot size ~330 μm FWHM). A moving transparent polyethylene tape protects the OAPM and polycapillary lens from Cu plasma debris. The OAPM, polycapillary lens, wire target, and tape assembly were placed inside a vacuum chamber evacuated to $\sim 10^{-2}$ mbar. The focused x-rays from the polycapillary lens exit the vacuum chamber through a 25-μm-thick Kapton window and then fall on the sample through a holed mirror (a 5 mm hole in the center). The holed mirror reflects the pump pulse, and both pump and probe pulse overlap at the sample in near collinear geometry (the angle between the pump and probe beams was ~2.5°). The pump beam uniformly photoexcites (heats) the sample as the laser spot size is much larger than the sample cross-section area (~0.7 × 1.0 mm^2, see Fig. S6). The transmitted diffracted x-rays from the single-crystal $EuTe_4$ sample (thickness t_{sample} ~10 μm) fall on a DRZ phosphor screen, and an electron-multiplying charge-coupled device (EMCCD, Make: Andor) measures the intensity. The TXRD pattern of $\mathbf{Q}_{CDW} = (2,2-|\mathbf{q}_{CDW}|,0)$ peak (see Fig. 3C, $|\mathbf{q}_{CDW}| = 0.643$ r.l.u., here r.l.u. refers to the reciprocal lattice unit) was recorded by varying the delay between the pump and probe pulses. To detect low-intensity signals and to decrease the Bremsstrahlung x-ray noise, the path between the x-ray source

and DRZ phosphor was shielded by 30-mm-thick lead sheets. To detect the small shift in the diffracted angle of the (2,0,0) Bragg peak due to heat deposition by the pump beam, EMCCD and DRZ phosphor screen were replaced by an x-ray CCD.

Inelastic x-ray scattering

High-resolution IXS experiments to measure wavevector-resolved dynamical structure factor $S(E)$ and phonon lifetimes of $EuTe_4$ were performed at beamline 30-ID-C (HERIX) [50–52] at the Advanced Photon Source. A small single crystal of approximately ~30 μm thickness was glued to a copper post using a high-temperature silver paste. The highly monochromatic x-ray beam of incident energy $E_i \simeq 23.7$ keV ($\lambda = 0.5226$ Å) had an energy resolution $\Delta E_i \sim 1.0$ meV (FWHM), and was focused on the sample with a beam cross-section ~35 × 15 μm (horizontal×vertical). The convoluted energy resolution of the incident x-ray beam and analyzer crystals was $\Delta E \sim 1.5$ meV. The sample mosaic measured on the HERIX instrument was less than 0.06°. The measurements were performed in the transmission geometry. Typical counting times were 20 to 150 s at each point in the energy scans at constant **Q**. The intensity vs. energy-transfer spectra were fitted with a damped harmonic oscillator (DHO) scattering function [53], subsequently convoluted with the measured instrumental resolution function, $R * S(E)$:

$$S(E) = A\,\frac{\left\{\frac{1}{2} \pm \frac{1}{2} + n(|E|)\right\} \times 2\Gamma E}{\left(E^2 - E_{ph}^2\right)^2 + (2\Gamma E)^2} + B, \quad (1)$$

where B is a constant background, $n(E)$ is the temperature-dependent Bose–Einstein distribution at energy transfer E, A is the amplitude, 2Γ is the FWHM of the phonon peak, and E_{ph} is the renormalized phonon energy in the presence of damping (the + sign is for $E > 0$, i.e., phonon creation, and the − sign is for $E < 0$, i.e., phonon annihilation).

Polarized Raman scattering

Raman spectroscopy experiments were performed using a Renishaw Raman spectrometer equipped with a confocal microscope in the backscattering geometry. The overall spectral resolution of the Raman spectrometer was ~1 cm^{-1}. Raman spectra were acquired using a 532 nm excitation source. The laser beam was focused on a beam diameter of 2 μm using a 50× objective

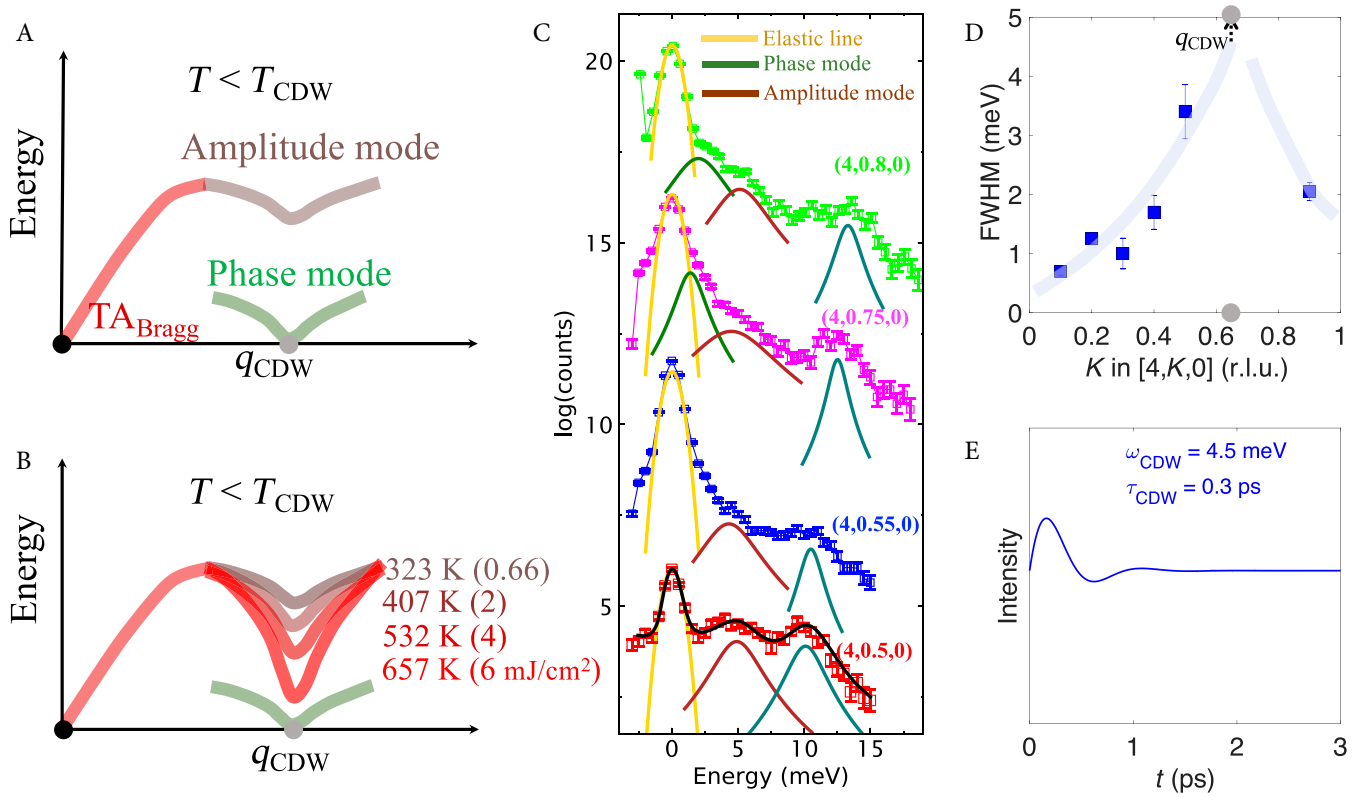

Fig. 2. Dynamics of the amplitude mode. (A) Qualitative illustration of phonon spectra below T_{CDW}. $\mathbf{q}_{CDW}$ denotes the CDW peak [see a gray color circle on the x-axis; for example, (4,0.643(1),0)] from which phase mode emerges. Transverse acoustic mode (TA_{Bragg}) emerges from the Bragg peak [see a black color circle on the x-axis; for example: (4,0,0)]. The amplitude mode appears as an optic mode above the CDW peak and is representative of the CDW order parameter. (B) Qualitative illustration of softening of the amplitude mode energy (ω_{AM}) on heating/photoexcitation. The ω_{AM} will drop to zero energy on higher fluence leading to the disappearance of the CDW peak and the emergence of the normal phase. (C) IXS measurements of the amplitude and phase mode near the $\mathbf{Q}_{CDW}$ at room temperature [9]. Fitted peaks without convolution with instrument resolution function are shown underneath the data (see details in the Inelastic x-ray scattering section). Note that the CDW peak intensity saturates the entire energy scan at $\mathbf{Q}_{CDW}$; hence, nearby **Q** points are shown. The excellent data statistics allow us to observe both phase and amplitude modes [for example, see **Q** = (4,0.8,0)]. Intensity is on the logarithmic scale. Error bars are from counting statistics ($\sqrt{N}$). (D) FWHM (2Γ) of the amplitude mode extracted by fitting the spectra shown in (C) using DHO. The FWHM diverges at $\mathbf{Q}_{CDW}$ due to nesting-driven electron–phonon coupling as discussed in Refs [7–9] and shown qualitatively by light blue lines. (E) The simulated time evolution of the amplitude mode using the measured $\omega_{AM(CDW)}$ and lifetime [$\tau_{AM(CDW)} = 1/(2\pi\Gamma)$].

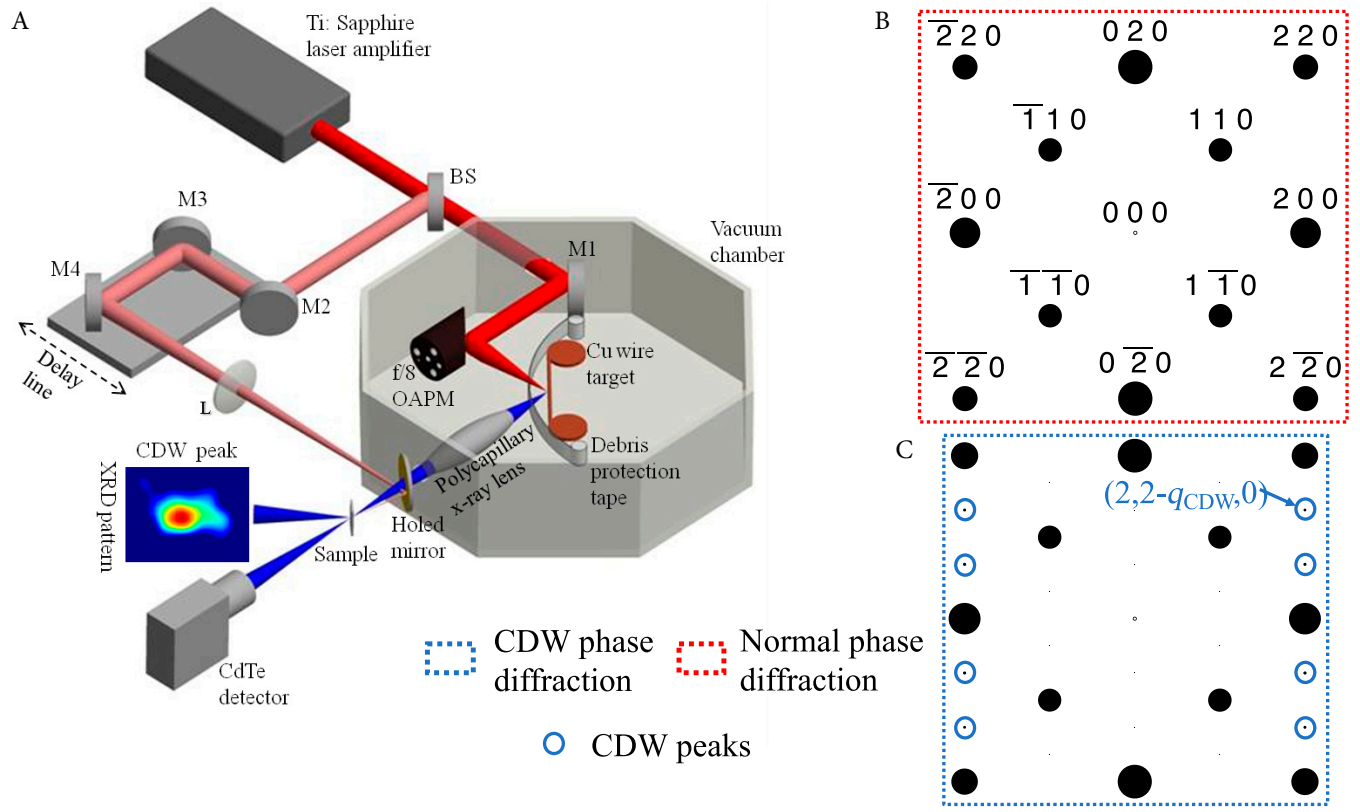

Fig. 3. TXRD experimental setup and CDW peaks. (A) Schematic of the TXRD setup used for optical pump and x-ray probe measurements. The diffracted x-rays are detected with an EMCCD detector. See details in the Methods section. (B) The simulated single-crystal XRD pattern of $EuTe_4$ in the normal phase in the $(H,K,0)$ scattering plane. The size of the black circle denotes the relative intensity of Bragg peaks. (C) Same as (B), except in the CDW phase. CDW peaks emerge between the Bragg peaks, as marked by blue circles corresponding to incommensurate $\mathbf{q}_{CDW}$. Higher-order CDW peaks are weaker than first-order CDW peaks and, consequently, are not visible in the panel. The Bragg peaks are not labeled in (C) as they are the same as in (B). TXRD data are measured for the $\mathbf{Q}_{CDW} = (2,2-|\mathbf{q}_{CDW}|,0)$, i.e.,(2,1.357,0) as indicated by the arrow.

lens. The laser power was kept below 10 μW to avoid laser-induced heating. Temperature-dependent Raman measurements were carried out by mounting the crystals in the Linkam TS 1500 stage with a temperature stability of ±0.1 K. Angle-resolved polarized Raman spectroscopy was carried out at room temperature by mounting the single crystal on a custom rotating stage. The incident light was plane-polarized, and the scattered beam was analyzed using an analyzer in parallel and cross-polarization geometry. In the present experiments, the incident laser beam propagates along the (001) direction of the $EuTe_4$ crystal and has light polarization in the (110) plane. The incident light polarization was rotated in-plane by rotating the crystal.

AIMD simulations

Electronic structure simulations were performed in the framework of density functional theory (DFT) as implemented in the Vienna Ab-initio Simulation Package (VASP 5.4.4) [54–56]. The details of structure relaxation, energy minimization, phonon simulation, and calculation of dynamical structure factor $S(\mathbf{Q},E)$ are the same as prior studies on $EuTe_4$ [8,9] Here, $\mathbf{Q}$ is the momentum transfer and $E = \hbar\omega$ is the phonon energy. The fidelity of simulations is confirmed by comparing AIMD simulations below $T < T_{CDW} \sim 726$ K [9] at 300 and 650 K on a $3 \times 3 \times 2$ supercell of the normal phase that incorporates the measured CDW distortion, i.e., same as the reported CDW phase in Ref. [48]. The supercell contains 180 atoms. AIMD simulations were performed using NVT-ensemble with Nośe-Hoover thermostat (MDALGO = 2). The simulations ran for 3,000 to 13,000 fs or more with a time step of 2 fs. Simulations were computationally expensive and ran for ∼168,000 and 72,000 CPU hours at 300 and 650 K on 240 cores. From the measured trajectory, the structure factor $S(\mathbf{Q})$ and intensity at $\mathbf{Q}_{CDW} = (2,2-|\mathbf{q}_{CDW}|,0)$ I_{CDW} were calculated. I_{CDW} was subsequently fast Fourier transformed to obtain the oscillation frequency of the amplitude mode (see Fig. 4). A standard zero padding was done before the fast Fourier transform (FFT).

Results and Discussion

Here, in the following subsections, firstly, we discuss the structure and CDW transition. Then, we measure the amplitude mode's energy and determine its polarization using meV-resolution IXS. Subsequently, we nonlocally probe the amplitude mode using TXRD at different fluences/temperatures, which we further confirm using polarized Raman scattering. Following this, we exclude the conventional electron and phonon heat diffusion as the possible reason for the nonlocal observation of the amplitude mode. Lastly, we invoke the possible formation of phonon–polariton and exciton–polariton to rationalize the observations.

Structure and CDW transition

Figure 1A and B shows the orthorhombic crystal structure of $EuTe_4$ in the normal phase (*Pmmn*). The layered structure along the *c*-axis is constituted of a Te bilayer and a Te monolayer

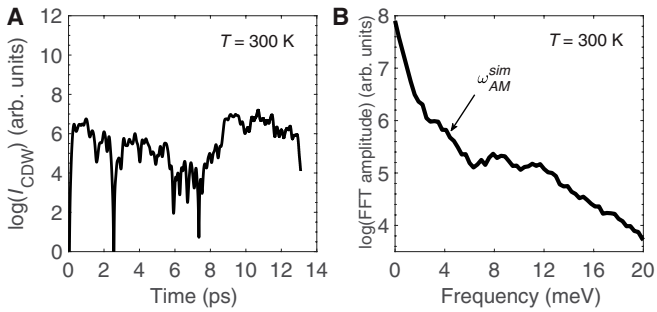

Fig. 4. Intensity modulation of CDW peak by the amplitude mode. (A) Intensity ($\log(I_{CDW})$) evolution of the CDW peak at $\mathbf{Q}_{CDW} = (2,2-|\mathbf{q}_{CDW}|,0)$ as extracted by calculating the square of the structure factor from AIMD trajectory at 300 K. (B) FFT amplitude versus frequency of intensity reported in (A). To improve the FFT signal, we have averaged FFT of eight CDW peaks, i.e., $\mathbf{Q}_{CDW} = (\pm 2, \pm 2 \pm |\mathbf{q}_{CDW}|,0)$. Similar to IXS experiments (see Fig. 2C), a broad amplitude mode near $\omega_{AM}^{sim} \sim$ 4 meV and high-frequency modes between 8 and 15 meV are visible. The frequency resolution is limited by trajectory length. Simulations were computationally expensive and ran for ~168,000 CPU hours at 300 K on 240 cores.

separated by the EuTe layer, i.e., (EuTe)-$\overline{\text{Te}}$-(EuTe)-$\overline{\overline{\text{Te}}}$-$\overline{\overline{\text{Te}}}$ – ⋯ [48]. Here, single and double overline imply Te atoms in monolayer and bilayer, respectively. Within the Te monolayer and Te bilayer, Te atoms form a square-net-like structure. The square-nets are inherently unstable and undergo planar distortion below T_{CDW} forming Te trimers as shown in Fig. 1C and D [9,20,48]. First-order transition at T_{CDW} on heating from room temperature and on cooling from $T > T_{CDW}$ are reported to be ~726 and 652 K, respectively [9]. The planar distortion is incommensurate with the underlying lattice occurring at $\mathbf{q}_{CDW} = (0,0.643(1),0)$ r.l.u. ($|\mathbf{q}_{CDW}| = 0.643$ r.l.u.). Other than the planar distortion, multiple CDW distortions along all crystallographic axes have been reported recently in the literature [9], but because of their proximity to Bragg peak or relatively smaller amplitude, we do not focus on them. Similar planar distortions are observed in the $R\text{Te}_2$ and $R\text{Te}_3$ family of compounds [12,13,19,23–28,30,57–59].

Momentum- and energy-resolved mapping of the amplitude mode

Incommensurate CDW phase leads to the appearance of two new modes emerging from $\mathbf{q}_{CDW}$, namely, phase and amplitude modes (akin to acoustic and optic modes), corresponding to purely tangential sliding and radial breathing emerge from the frozen lattice distortions, as pictorially illustrated in Fig. 2A. In the pictorial depiction, the Bragg and CDW peak are to be taken as (4,0,0) and (4,0.643(1),0), respectively. Transverse acoustic mode emanates from the Bragg peak as it would in the normal phase. On heating, the amplitude mode energy (ω_{AM}) decreases and will drop to zero at $T_{CDW} \sim 726$ K leading to stabilization of the normal phase, as shown in Fig. 2B. We directly map all the excitation in the CDW phase using IXS measurements at room temperature (data from Ref. [9]). Figure 2C shows $S(E)$ of $EuTe_4$ near the $\mathbf{Q}_{CDW} = (4,0.643(1),0)$. Note that the CDW peak intensity saturates the entire energy scan at $\mathbf{Q}_{CDW}$; hence, nearby $\mathbf{Q}$ points are shown. The excellent data statistics allow us to observe both phase and amplitude modes emanating from $\mathbf{Q}_{CDW}$ and are marked in the figure [for example, see $\mathbf{Q} = (4,0.8,0)$]. Importantly, the observation of the amplitude mode along [4,*K*,0] confirms the predicted polarization using phonon simulations, i.e., *a*-polarized transverse phonon propagating along the [0,1,0] direction in the reciprocal space, see Ref. [8]. We fit $S(E)$ using DHO (see the Methods section) to extract phonon energy ($E = \hbar\omega$) and linewidth (2Γ, FWHM). We find ω_{AM}^{IXS} near $\mathbf{Q}_{CDW}$ to be ~4.5 meV (see Ref. [9] for the measured amplitude mode dispersion curve). Other high-energy modes are present between 8 and 15 meV. The FWHM of the amplitude mode for the entire Brillouin zone (along [4,*K*,0] $\forall$ $0 < K < 1$ r.l.u.) is shown in Fig. 2D. As expected, FWHM diverges at $\mathbf{Q}_{CDW}$ due to nesting-driven electron–phonon coupling as discussed in Refs [7–9] and shown qualitatively by light blue lines. Since E_{AM}^{IXS} is the same magnitude as FWHM, the amplitude mode is overdamped. From the data, if we take 2Γ to be 4.5 meV at $\mathbf{Q}_{CDW}$, then the lifetime τ of the mode becomes 0.3 ps ($\tau = 1/2\pi\Gamma$). If we were to observe the amplitude mode as oscillations in any time-resolved measurements, its amplitude would diminish rapidly due to small τ (see Fig. 2E).

Time-resolved mapping of the amplitude mode

The amplitude mode was observed for photoexcited $SmTe_3$ appearing as oscillations in the intensity of the CDW peak [31]. We follow the same experimental protocol, except the measurements are in transmission mode as opposed to grazing incidence reflection geometry in Ref. [31]. However, before measurements, we first perform the AIMD simulations to simulate dynamical structure factor $S(\mathbf{Q},E)$ in multiple Brillouin zones [8]. The $S(\mathbf{Q},E)$ simulations enable us to identify the wavevectors that have large oscillations corresponding to the amplitude mode and are accessible within the physical constraints of our experimental setup (not blocked by vacuum chamber and lead sheets). We find measurable intensity of the amplitude mode oscillations at $\mathbf{Q}_{CDW} = (2,2-|\mathbf{q}_{CDW}|,0)$, i.e., (2,1.357,0) peak isolated from other modes (see Fig. 4A). Consistent with IXS measurements (see $\mathbf{Q} = (4,0.55,0)$ and (4,0.75,0) in Fig. 2C), the Fourier transform of intensity (Fig. 4B) shows a broad peak at $\omega_{AM}^{sim} \sim 4$ meV and high-frequency modes between 8 and 15 meV. Here, we note two points. Firstly, we probed the amplitude mode in IXS measurements along [4,*K*,0] owing to its large intensity and along [2,*K*,0] in TXRD measurements due to the physical constraints of the setup; however, amplitude mode dynamics is identical in both Brillouin zones. Secondly, phonon intensity in IXS measurements at $\mathbf{Q}_{CDW}$ or in close vicinity is not visible because of strong CDW peak intensity; hence, we compare TXRD measurements with nearby $\mathbf{Q}_{CDW}$ points. The comparison with nearby points is remarkable as the amplitude mode disperses weakly, i.e., nearly flat dispersion at room temperature [9].

We use TXRD in the transmission geometry to measure the time-resolved evolution of the intensity at $\mathbf{Q}_{CDW} = (2,2-|\mathbf{q}_{CDW}|,0)$ with respect to delay between optical pump and x-ray probe pulses (see Fig. 3A and the Methods section). Note that all Bragg peak, plane, and direction notations refer to the normal phase. The advantage of using x-rays as opposed to optical probe pulse is that owing to the momentum conservation, modes with wavevector $\mathbf{Q}_{CDW}$ only will contribute to measured oscillations. The $\mathbf{Q}_{CDW}$ CDW peak appears below T_{CDW} owing to condensation of the planar distortion as discussed earlier (see Fig. 3B and C). The other first-order CDW peaks in the (*H*, *K*, 0) plane are circled in Fig. 3C. The first-order CDW peaks are at least an order of magnitude weaker than the nearest

Bragg peak [9]. The higher-order CDW peaks, for example, (2,2|$\mathbf{q}_{CDW}$|,0), are not visible in Fig. 3C because of even lower intensity (size of black circles indicates relative intensity) [9]. The low intensity at $\mathbf{Q}_{CDW}$ necessitates a collection time of 300 s per delay point. Figure 5A shows measured oscillations in the intensity for a fluence of 4 mJ/cm^2. The measurements were repeated to ensure the reproducibility of extracted oscillation frequency.

To extract one or more oscillation frequencies from the data, we can perform a FFT or fit (un)damped sinusoidal function(s). We used both methods to extract the oscillation frequency, yielding nearly identical results. The black solid line in Fig. 5A shows the extracted oscillation frequency ω_{AM}^{TXRD} at ~2.6 meV (or equivalently ω_{AM}^{TXRD} ~0.6 THz) by fitting the sinusoidal function. Here, ω_{AM}^{TXRD} was kept as fitting parameter. Similarly, the FFT amplitude of the measured signal (see Fig. 5B) shows a peak centered around ~2.6 meV, consistent with the sinusoidal fitting. From the fitting in Fig. 5A, we observe that the single frequency at ~2.6 meV does not capture high-frequency oscillations visible in the data. The high-frequency oscillations originate from high-energy phonon mode at $\mathbf{Q}_{CDW}$ (present between 8 and 15 meV, see Figs. 2C and 4B) having an oscillation period T between 250 and 500 fs [$T = 1/\omega$ (in units of THz), 1 THz = 4.1357 meV]. Since our x-ray probe pulse has a pulse width of ~300 fs, the high-frequency oscillations are not resolvable and appear as noise. Note that intensity quenching or recovery is not observed on photoexcitation, as in the transmission geometry, probe region (~10 μm) is approximately 65 times larger than the photoexcited region (~145 nm). We compare the fitted oscillation frequency from TXRD measurements, i.e., the ω_{AM}^{TXRD} to ω_{AM}^{IXS}, and find that ω_{AM}^{TXRD} is less than the measured ω_{AM}^{IXS} (~4.5 meV) and simulated ω_{AM}^{sim} (~4 meV) at room temperature. As discussed earlier, since ω_{AM} decreases on heating, we first explicitly calculate the temperature rise on laser pumping to understand the origin of the measured difference from the two techniques.

We measured the peak shift of (2,0,0) on photoexcitation with the same fluence. For high-resolution $\Delta 2\theta^{\circ}$ measurements, we replaced phosphor and EMCCD with x-ray CCD. Figure 5C shows $\Delta 2\theta^{\circ}$ as a function of delay. Each delay point was measured for 120 s, during which 120,000 laser pulses fell on the sample. Due to low thermal conductivity ($\kappa < 1$ Wm^{-1}K^{-1} at 300 K, see details later in the text), the sample cannot dissipate heat (the only possible heat dissipation is via air convection and conduction via a small contact region on copper post). The heat gets accumulated and leads to a rise in sample temperature. The peak shift, signifying the rise in sample temperature, remains nearly constant after measurements of one delay point for 120 s as laser heating reaches equilibrium with heat dissipation. Since the measurements are performed in transmission geometry, it indicates that the entire sample thickness of ~10 μm is uniformly heated after a few initial laser pulses. We compared the (2,0,0) peak shift with T-dependent synchrotron XRD data to determine the temperature rise (ΔT) and found it to be 236±24 K (see Section S4). Hence, the lower value of measured ω_{AM}^{TXRD} is possibly owing to the heating of the sample, which we confirm below.

We repeated the measurements at different fluences to confirm whether the sample heating occurs for all cases and whether the measured oscillations originate from the amplitude mode. ω_{AM}^{TXRD} must approach ω_{AM}^{IXS} ~4.5 meV for low fluences (as T will be close to room temperature) and decrease on increasing fluence (see illustration in Fig. 2B). Figure 6A and B shows the TXRD data with fitted oscillations and FFT amplitude for a fluence of 2 mJ/cm^2 (data for other fluences is shown in Fig. S5). All fluences lead to uniform sample heating (see Section S4). The sample temperature $T = (297 + \Delta T)$ K determined from shift in $\Delta 2\theta^{\circ}$ for fluence of 2 mJ/cm^2 is indicated on the panel. The fitted ω_{AM}^{TXRD} for all measured fluences is shown in Fig. 6C. As we can observe, the ω_{AM}^{TXRD} decreases on increasing fluence and, as expected, approach ω_{AM}^{IXS} ~4.5 meV at low fluences. Note that in measurements on photoexcitation, electronic temperature rises above T_{CDW} and reaches equilibrium with lattice in few picoseconds depending on the fluence (see details in the Heat diffusion on photoexcitation section); hence, the oscillations at ω_{AM} are triggered once the CDW phase recovers. In particular, for the fluence of 6 mJ/cm^2, oscillations are observed after ~3 ps, when equilibrium is reached (see Fig.

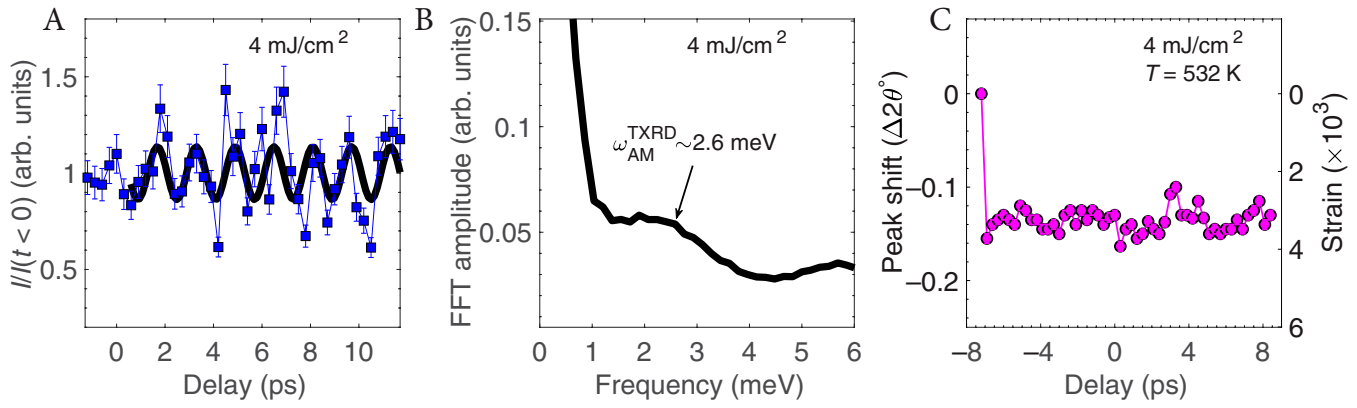

Fig. 5. Time-resolved response of the amplitude mode. (A) TXRD intensity ($I/I(t<0)$) at $\mathbf{Q}_{CDW}$ = (2,2−|$\mathbf{q}_{CDW}$|,0) CDW peak (blue square markers) as a function of delay between the 800 nm pump and x-ray probe pulses for a fluence of 4 mJ/cm^2. A solid black line denotes the oscillations corresponding to the fitted amplitude mode frequency component in the measured data. The high-frequency components between 8 and 15 meV are not resolvable in our data due to the large (300 fs) FWHM of the x-ray probe pulse (see Fig. 4B and discussion in the text). Error bars are from shot-to-shot fluctuations. (B) FFT amplitude versus frequency of intensity reported in (A). A peak corresponding to the amplitude mode centered near 2.6 meV is marked by an arrow. (C) Peak shift (strain) of the (2,0,0) Bragg peak as a function of delay. Each data point is measured for 120 s. The constant peak shift after the first delay point indicates the rise in the equilibrium sample temperature, as indicated in the panel.

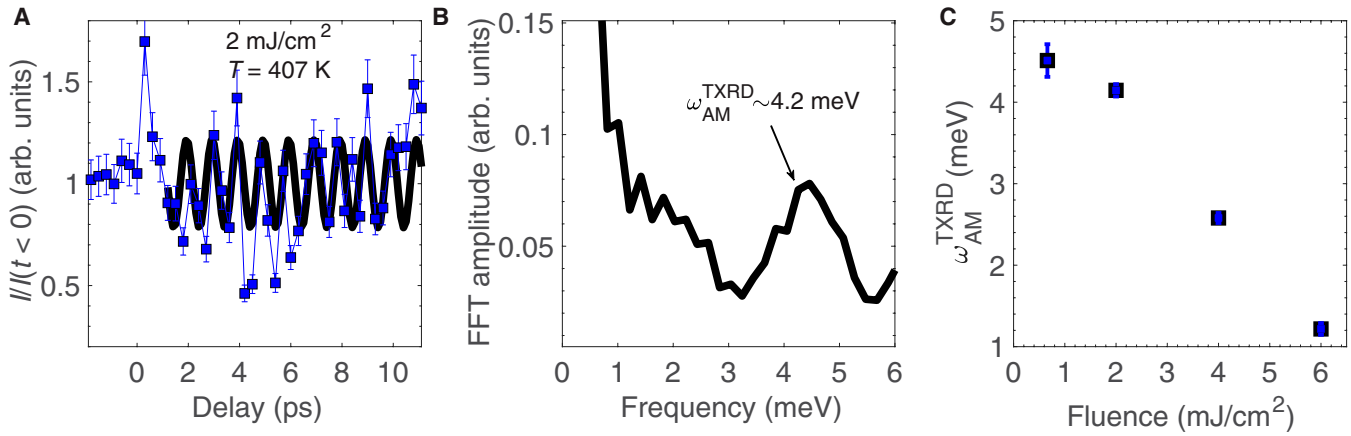

Fig. 6. Time-resolved response of the amplitude mode for different fluence. (A) Time-resolved x-ray diffraction intensity at $\mathbf{Q}_{CDW}$ = (2,2−|$\mathbf{q}_{CDW}$|,0) CDW peak (blue square markers) as a function of delay between the 800 nm pump and x-ray probe pulses for a fluence of 2 mJ/cm^2. Due to the low κ, the fluence leads to rise in the equilibrium sample temperature, as indicated in the panel. A solid black line denotes the oscillations corresponding to the fitted frequency component in the measured data. The high-frequency components between 8 and 15 meV are not resolvable in our data due to the large (300 fs) FWHM of the x-ray probe pulse (see Fig. 4B and discussion in the text). Error bars are from shot-to-shot fluctuations. (B) FFT amplitude versus frequency of intensity reported in (A). A peak corresponding to the amplitude mode centered near 4.2 meV is marked by an arrow. (C) The amplitude mode energy (ω_{AM}^{TXRD}), extracted from the fitting of measured data, as a function of fluence. The data for a fluence of 6 mJ/cm^2 are shown in Fig. S5. The amplitude mode energy converges to ~4.5 meV at low fluence, consistent with the value reported using meV-resolution IXS at 300 K. Error bars (one standard deviation on either side of the markers) are obtained from fitting the sinusoidal function.

S5A). Consequently, the phase of the oscillations is dependent on CDW phase recovery that varies from sub-picosecond to few picoseconds in rare-earth tellurides [23,31].

Temperature dependence of the amplitude mode

To unambiguously confirm that the observed T dependence of the measured oscillations originates from the amplitude mode, we can independently probe the amplitude mode using Raman or infrared (IR) scattering, as the CDW phase is non-centrosymmetric [48]. We perform polarized Raman scattering on a single crystal of $EuTe_4$ oriented such that the [001] crystallographic direction points along the laser propagation direction and laser polarization is in the (110) plane. For the measured configuration, only A_g modes will have non-zero Raman intensity (see Section S2). Figure 7A shows the Raman spectrum for c(aa)$\bar{c}$ parallel polarization geometry. Here c and $\bar{c}$ refer to the incident and outgoing laser propagation direction, and (aa) denotes the incident and outgoing laser polarization. The parallel polarization geometry implies incident and outgoing laser polarization are identical (for the cross-polarization geometry, incident and outgoing laser polarization are orthogonal). As indicated in the figure, we resolve 7 modes at room temperature, including the amplitude mode (mode 1). In the normal parent phase, 5 A_g modes are present; hence, some observed modes are folded back from $\mathbf{q}_{CDW}$ to the zone center in the CDW phase. We can differentiate the normal phase modes from CDW phase modes by angle-resolved polarized Raman scattering in parallel and cross-polarization geometry. Figure 7E and F shows an apparent four-fold symmetry for mode 7 in both parallel and cross-polarization geometry with a 45° phase difference as expected for the A_g mode. In contrast, a two-fold symmetry is observed for modes 5 and 6, suggesting their origin from the band folding in the CDW phase. The other modes have a relatively weak intensity to identify their two- or four-fold symmetry. Figure 7B shows the T evolution of the Raman spectrum, highlighting phonon softening and broadening. We fit all modes with the Lorentzian function to extract the energy and linewidths. The extracted T dependence of ω_{AM}^{Raman} and $2\Gamma_{AM}^{Raman}$ is shown in Figure 7C and D, respectively. Consistent with IXS measurements and AIMD simulations, the amplitude mode is overdamped. The observed softening of ω_{AM}^{Raman} is similar to T dependence from TXRD measurements (see Fig. 6C), thus confirming that oscillations in TXRD data for different fluences indeed originated from the amplitude mode.

However, two questions arise from the above observations. First, IXS and Raman measurements and AIMD simulations show that the amplitude mode is overdamped, but the observed TXRD oscillations are underdamped. FFT in Fig. 6B confirms the underdamped nature as the amplitude mode's linewidth (FWHM~0.9 meV) is nearly five times smaller than its energy (ω_{AM}^{TXRD} ~4.2 meV) and substantially less than the FWHM from IXS measurements (see Fig. 2C). The second is the sample is photoexcited to a penetration depth δ ~145 nm (see Section S7), but in the transmission geometry, x-rays probe the entire thickness of t_{sample} ~10 μm. Moreover, the heat cannot propagate to more than 3δ from electron and phonon diffusion till 20 ps, as discussed below. Hence, it remains to be identified how the amplitude mode propagates through the material with a velocity far exceeding the acoustic strain pulse velocity with little damping. Below, we discuss both questions in detail.

Heat diffusion on photoexcitation

Firstly we discuss heat diffusion via electrons and phonons. We use the two-temperature model to simulate the heat transfer from the pump pulse to photoexcited electrons and subsequently to phonons via electron–phonon coupling [60]. To confirm the fidelity of the two-temperature model, we also simulate phonon diffusion by solving the Boltzmann transport equation (BTE) using experimentally determined phonon energies (E_{ph}), group velocities (v_g), and lifetimes (τ) [61]. See Section S9 for a description/parameters of the two-temperature model. Figure 8A shows the

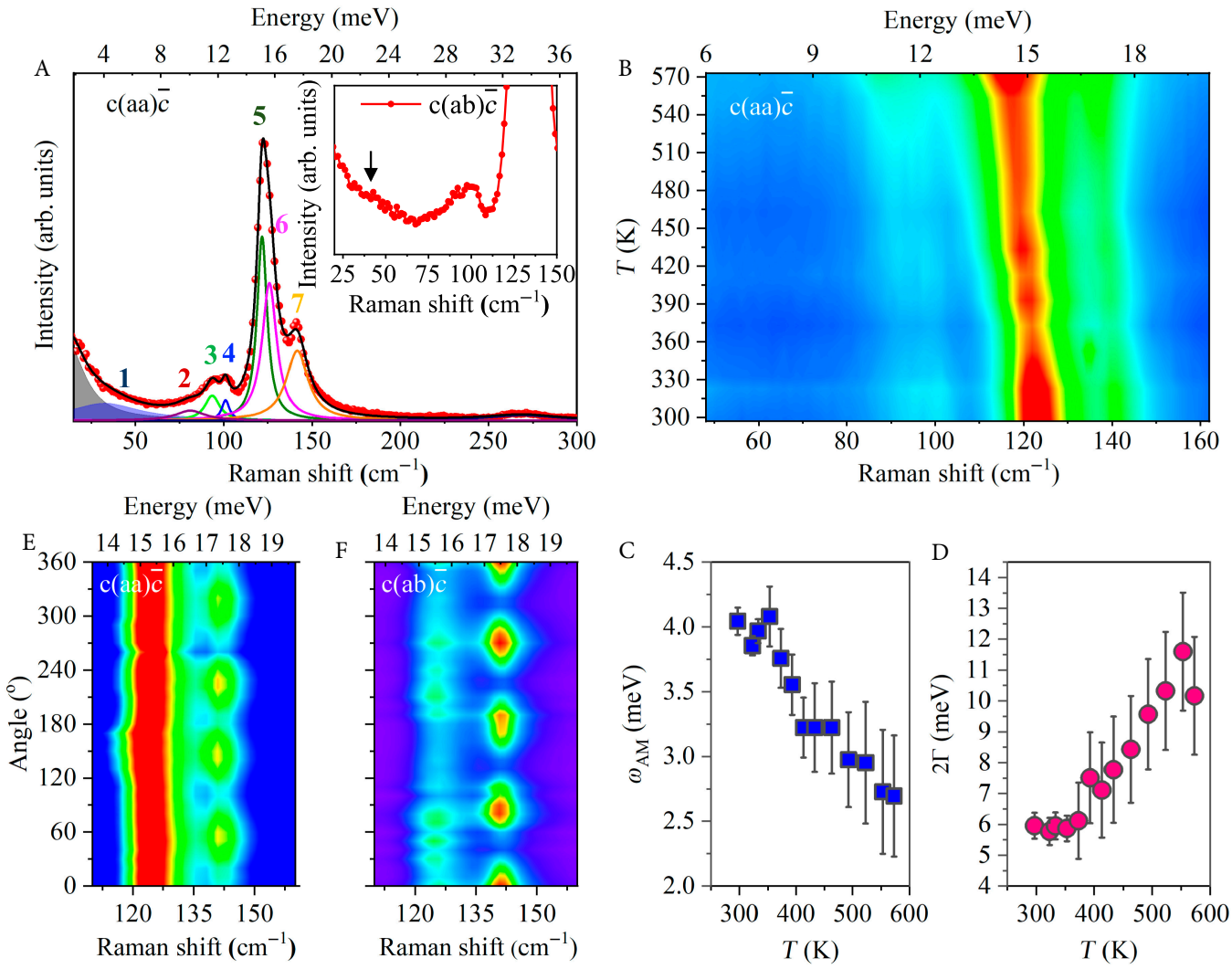

Fig. 7. Polarized Raman scattering of the amplitude mode. (A) Raman spectrum of $EuTe_4$ for c(aa)$\bar{c}$ parallel polarization geometry at 300 K. Rayleigh scattering (gray shaded area), amplitude mode (blue shaded area, peak 1), and other phonon modes fitting are shown underneath the data. Inset shows the overdamped amplitude mode (marked by an arrow) for c(ab)$\bar{c}$ cross-polarization geometry at 300 K. (B) Temperature evolution of Raman spectrum in the same measured configuration as (A). (C and D) ω_{AM} and 2Γ as a function of temperature obtained from fitting the amplitude mode. Error bars (one standard deviation on either side of the markers) are obtained from fitting the Lorentzian function. (E and F) Color map of angular-resolved Raman spectra at 300 K in parallel polarization (E) and cross-polarization (F) geometry. Measurements show an apparent four-fold symmetry for peak 7 in both parallel and cross-polarization geometry with a 45° phase difference between them as expected for A_g symmetry mode, while for peak 6, such four-fold symmetry is absent, suggesting band folding from $\mathbf{q}_{CDW}$ to the zone center owing to the CDW distortion.

temperature profile post-pump pulse of fluence 6 mJ/cm^2. For the 800 nm laser pump pulse, δ is 145 nm (see Section S7). Electronic temperature (T_e) along the orange arrow in Fig. 8A for different delay times is shown in Fig. 8B. As we can observe, T_e rises rapidly post-pump pulse. The temperature rise can be seen up to a depth of 1 μm. As heat is transferred to the phonons via electron–phonon coupling and diffuses, the peak T_e drops below 400 K at 5 ps. Phonon temperature (T_{ph}) rises above 400 K in the first few picoseconds (see Fig. S7) and subsequently diffuses. Furthermore, we solve BTE using E_{ph}, v_g, and τ as input. E_{ph} and v_g are taken from Ref. [9], while measured τ using IXS are reported in Fig. 8C. For a δ of 145 nm, T_{ph} rises above room temperature to a depth of ~300 nm due to electron–phonon coupling. For BTE simulations, we assume this rise in T_{ph} as the initial condition. As we can observe from Fig. 8D (see blue circles), because of ultralow phonon thermal conductivity ($\kappa < 1$ Wm^{-1}K^{-1} at 300 K, calculated as [62,63] $\kappa = \frac{1}{3} C_v v_g^2 \tau$ using experimental data) of $EuTe_4$, the phonon diffusion is extremely slow. Consequently, heat diffuses to approximately 20 nm further than the initial ~300 nm. Even if we assume all phonons travel ballistically or fictitiously scale the κ by order of magnitude by increasing v_g, still furthest the heat diffuses to approximately 500 nm from the sample surface. From the above simulations, it is apparent that for realistic parameters, the heat diffusion from incident laser pulse is limited to 2 or 3 times the penetration depth up to the measured delay time, substantially less than the sample thickness ($3\delta/t_{sample} \sim 0.04$). Consequently, the acoustic strain pulse generated from sample heating [64] will contribute little to diffracted x-rays in the transmission geometry as the heating is limited to a small depth only. Moreover, as described earlier, our direct strain measurement did not show any laser pump-induced change for positive delays (see Fig. 5C), thus further confirming that acoustic strain pulse did not contribute to the measured oscillations.

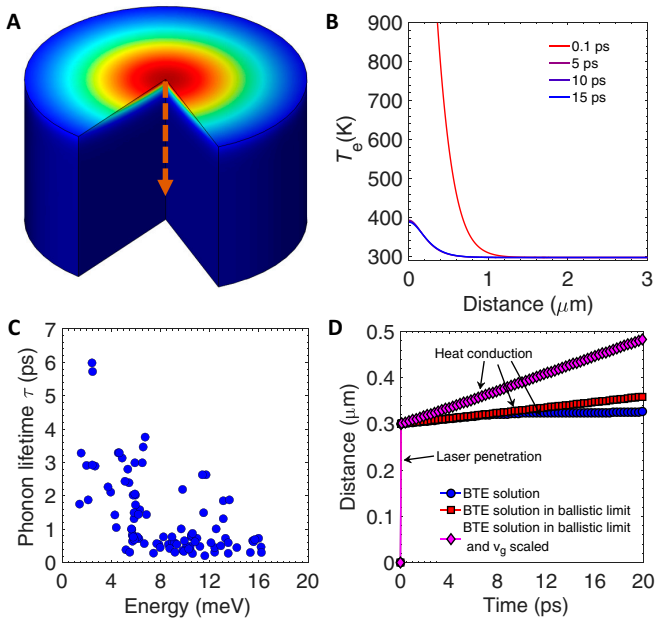

Fig. 8. Heat diffusion via electrons and phonons. (A) Schematic illustration of temperature profile post-laser excitation on $EuTe_4$ sample at $t = 0$. The laser penetration depth is $\delta \sim 145$ nm. The orange arrow denotes the heat propagation direction shown in (B) and (D). (B) Electronic temperature (T_e) as a function of heat propagation distance for various time delays obtained using the solution of the two-temperature model. (C) Measured phonon lifetime (τ) using IXS as a function of phonon energy. (D) Heat diffusion by phonons [along the orange arrow shown in (A)] as a function of time post-arrival of the laser pulse. Because of the large δ, the initial temperature rises to a depth of ~0.3 μm. BTE solution denotes the solution of phonon Boltzmann transport equation using phonon dispersions and measured τ [see (C)], BTE solution in the ballistic limit refers to the case when $\tau \rightarrow \infty$, and BTE solution in ballistic limit and v_g scaled is the same as the earlier case except, here, v_g is also scaled by a factor of 3.

Coupling of the amplitude mode with pump photon

Amplitude mode can be created by another mechanism, as discussed in the literature [31,41,65]. Since the laser pumping (photoexcitation) destroys (or reduces the distortion amplitude) the CDW [19,23,31], it abruptly changes the interatomic potential; consequently, the frozen lattice distortions are thawed and propagate as amplitude mode in the sample [31,41,65]. The dynamics of the propagating amplitude mode is typically modeled using a time-dependent extension of the Ginzburg–Landau formalism that reduces to the commonly used displacive excitation of coherent phonons in low-fluence limit [31]. Similar to other rare-earth tellurides [31,39], the amplitude mode in $EuTe_4$ is released by CDW melting. On propagation, the overdamped amplitude mode will decay rapidly, as discussed earlier (see Fig. 2E). However, our measurements show underdamped nature, thus indicating the coupling of amplitude mode with other excitations leading to long-lived quasiparticles. Phonon–polariton [42,45,46,66–69] and exciton–polariton [43,70–72] are two quasiparticles that can travel with light-like speed beyond the laser penetration depth and heat diffusion region and have long lifetimes. Other possibilities may exist but we are not aware of those. Below, we explore both scenarios.

The amplitude mode can couple with an IR photon to form a phonon–polariton; however, it must be polar (symmetry-odd). Phonon–polariton quasiparticles are reported in ferroelectrics $LiTaO_3$ [45,46] and $LiNbO_3$ [42], where they are found to propagate with little dissipation at light-like speed to distances exceeding 50 μm. Using group theory and symmetry analysis of $EuTe_4$, we explicitly calculate the symmetry vectors of the irreducible representation of the CDW phase and projected symmetry vectors to the eigenvectors of the unstable modes of the normal phase. We identify that the unstable modes at wavevectors $\mathbf{q}_{CDW}$ of the normal phase transform to A1 and B1 character polar (symmetry-odd) modes in the CDW phase, thus confirming that the amplitude mode is polar in the CDW phase (see Section S10 for detailed description). Consequently, as discussed above, the polar nature of the amplitude mode potentially enables coupling with an IR photon to form a phonon–polariton, wherein propagating polariton wave triggers the amplitude mode as it travels through the thickness. Specifically, for an uncharged medium, the interaction of a polar phonon mode and an IR photon can be described by Maxwell's equation:

$$\nabla \cdot \mathbf{D} = 0, \tag{2}$$

where $\mathbf{D}$ is the electric displacement vector. For a plane wave with wavevector $\mathbf{k}$, Eq. 2 can be written in terms of electric field $\mathbf{E}$ as

$$\epsilon(\omega)(\mathbf{k} \cdot \mathbf{E}) = 0. \tag{3}$$

Here, $\epsilon(\omega) = \epsilon_\infty \frac{\omega_{LO}^2 - \omega^2}{\omega_{TO}^2 - \omega^2}$ is the dielectric constant of the material. Two solutions of Eq. 3, i.e., $\epsilon(\omega) = 0$ and $\mathbf{k} \cdot \mathbf{E} = 0$, correspond to longitudinal optic ω_{LO} and transverse optic ω_{TO} resonance frequency, respectively. Using $|\mathbf{k}|^2 = \frac{\omega^2}{c^2}\epsilon(\omega)$, we can obtain dispersion relation of phonon–polariton,

$$\omega^2 = \frac{1}{2\epsilon_\infty}\left\{c^2|\mathbf{k}|^2 + \epsilon_\infty\omega_{LO}^2 \pm \sqrt{\left(c^2|\mathbf{k}|^2 + \epsilon_\infty\omega_{LO}^2\right)^2 - 4\epsilon_\infty c^2|\mathbf{k}|^2\omega_{TO}^2}\right\}. \tag{4}$$

For $EuTe_4$, ω_{TO} corresponds to ω_{AM} (a-polarized transverse phonon propagating along the [0,1,0] direction in the reciprocal space, see Refs. [8,9]) and splitting between ω_{TO} and ω_{LO} is small. Figure 9C qualitatively illustrates the formation of phonon–polariton as given by Eq. 4 (ω_{LO} is not shown for clarity). Note that between ω_{LO} and transverse ω_{TO} (i.e., reststrahlen band), the real part of $\epsilon(\omega)$ is negative; hence, waves are exponentially attenuated [42]. As we can observe, the energy of phonon–polariton at $\mathbf{q}_{CDW}$ is similar to the amplitude mode. Hence, the observed oscillations in the TXRD data have the same energy and T dependence as that of the amplitude mode.

The other possibility is the formation of exciton–polariton. $EuTe_4$ possesses linearly dispersing p bands near the Fermi energy (E_F) [8,21,48], which enables the formation of a large number of electron–hole pairs with same $\mathbf{q}$. We illustrate this scenario in Fig. 9A. Two linearly dispersing bands (shown with red color lines, similar to dispersion in $EuTe_4$ [8]) of opposite Fermi velocity (v_F) cross E_F at $(\mathbf{k}, \epsilon_\mathbf{k})$ and $(\mathbf{k}', \epsilon_{\mathbf{k}'})$. Here, $\mathbf{k}' = \mathbf{k} + \mathbf{q}$, $\epsilon_\mathbf{k} = \epsilon_{\mathbf{k}'} = E_F$, and $v_{F,\mathbf{k}} \simeq -v_{F,\mathbf{k}'}$. The magnitude of $\mathbf{q}$ is shown as a blue color line joining $(\mathbf{k}, \epsilon_\mathbf{k})$ and $(\mathbf{k}', \epsilon_{\mathbf{k}'})$. Now, if we select two new $\mathbf{q}$ points $(\mathbf{k} + \Delta\mathbf{k}, \epsilon_\mathbf{k} + v_{F,\mathbf{k}}\Delta\mathbf{k})$ and $(\mathbf{k}' + \Delta\mathbf{k}, \epsilon_{\mathbf{k}'} + v_{F,\mathbf{k}'}\Delta\mathbf{k})$ above and below E_F (shown by green color circles), we find that new points are also separated by the same $\mathbf{q}$. Thus, due to the linear dispersion, multiple electron–hole pairs can be formed at the same $\mathbf{q}$. The

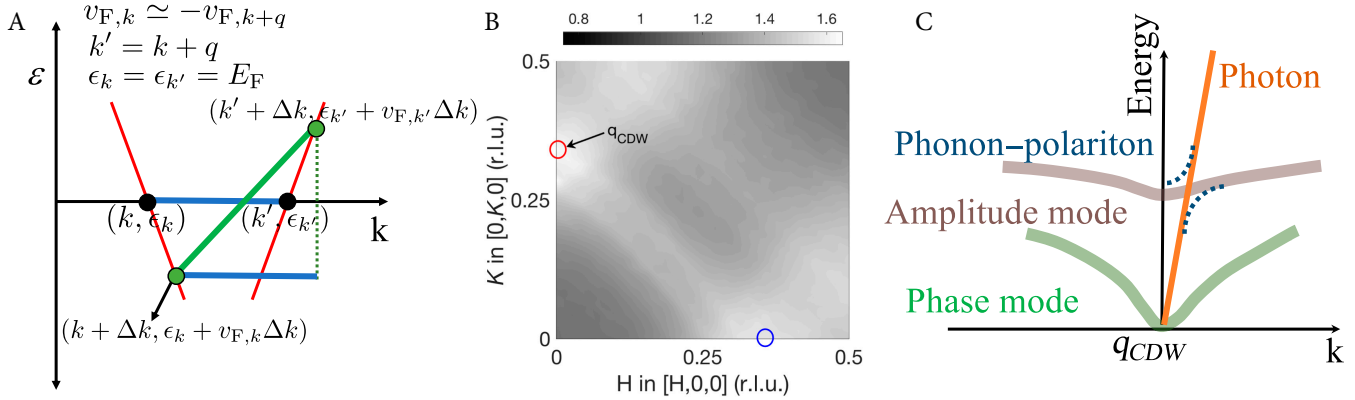

Fig. 9. Lindhard susceptibility and formation of exciton–polariton and phonon–polariton. (A) Pictorial depiction of electronic states near E_F contributing to the real part of Lindhard susceptibility Re{$\chi_0(\mathbf{q})$} at wavevector $\mathbf{q}$ (blue line). Here, owing to linear dispersion near E_F (red curves), the electronic states above and below E_F (green line) also contribute to the divergence of Re{$\chi_0(\mathbf{q})$} at the same $\mathbf{q}$. (B) Calculated Re{$\chi_0(\mathbf{q})$} in the $(H,K,0)$ reciprocal space showing a peak at $\mathbf{q}_{CDW}$ [marked by the red circle at (1−| $\mathbf{q}_{CDW}$|), i.e., 0.357 r.l.u.] along the K direction. The peak along H (marked by the blue circle) is relatively weak [8]. (C) Qualitative illustration of coupling between incoming photon and polar amplitude mode, leading to the propagation of the phonon–polariton quasiparticle in the material.

electron–hole pair formation leads to the divergence of electron–hole polarizability $\chi_0(\mathbf{q})$ and is shown to be the origin of CDW in $EuTe_4$ [8]. Similar to the previous study [8], we explicitly calculate the real part of $\chi_0(\mathbf{q})$ [2]

$$\mathrm{Re}\{\chi_0(\mathbf{q},\omega)\} = \lim_{\gamma\to 0}\frac{e^2}{\Omega}\sum_{\mathbf{k}}\sum_{l,l'} \frac{\left(\epsilon_{\mathbf{k}+\mathbf{q},l'} - \epsilon_{\mathbf{k},l} - \hbar\omega\right)\left(f\left(\epsilon_{\mathbf{k}+\mathbf{q},l'}\right) - f\left(\epsilon_{\mathbf{k},l}\right)\right)}{\left(\epsilon_{\mathbf{k}+\mathbf{q},l'} - \epsilon_{\mathbf{k},l} - \hbar\omega\right)^2 + \gamma^2} |\langle \mathbf{k}+\mathbf{q}, l' | V | \mathbf{k}, l\rangle|^2, \quad (5)$$

where e is the electron charge, Ω is the system volume, $f(\epsilon_{\mathbf{k},l})$ denotes the electron's Fermi distribution function at energy ϵ for a given wavevector $\mathbf{k}$ and a band index l, $|\langle \mathbf{k}+\mathbf{q}, l' | V | \mathbf{k}, l\rangle|^2$ is the matrix transition elements between states $\langle \mathbf{k}+\mathbf{q}, l' |$ and $|\mathbf{k}, l\rangle$, and γ is an infinitesimal constant representing broadening. The first and second summation represents the sum over all $\mathbf{k}$ states and all bands l in the first Brillouin zone, respectively. The calculated Re{$\chi_0(\mathbf{q})$} is shown in Fig. 9B. Using blue and red circles, we mark the maxima along H and K reciprocal space directions, respectively. The peak along K occurs at $\mathbf{q}_{CDW}$. Thus, we can conclude that $EuTe_4$ forms abundant electron–hole pairs, i.e., excitons at $\mathbf{q}_{CDW}$. The excitons can couple with photons to form exciton–polariton quasiparticles [43,70–72]. Exciton–polariton can propagate to macroscopic distances exceeding 50 μm, as observed for $CsPbBr_3$ perovskite microwire microcavity at room temperature [70]. On photoexcitation, excitons will break, thus triggering the melting of CDW and the release of the amplitude mode. As discussed above, propagation of both phonon–polariton and exciton–polariton is a possibility. However, long coherences for exciton–polariton are generally observed for microcavity architecture [70,72] or at low temperatures [71]. On the other hand, phonon–polariton can propagate coherently for macroscopic distances in single crystals at room temperature [42,45,46]. Although our measurements and simulations cannot conclusively confirm or rule out one scenario, nevertheless measured oscillations are likely from propagating phonon–polariton.

Conclusion

In summary, we have characterized the polar amplitude mode in $EuTe_4$ using meV-resolution IXS, polarized Raman scattering, TXRD in the transmission geometry combined with AIMD simulations of amplitude dynamics, simulation of electron–hole polarizability, group theory, and symmetry analysis. The pump-induced oscillations of the CDW peak intensity occur at ω_{AM} and show underdamped nature. The underdamped oscillations are at odds with the overdamped amplitude mode measured using IXS measurements and polarized Raman scattering. The observed behavior can be rationalized by coupling of the polar amplitude mode with incident infrared photons to form a phonon–polariton quasiparticle that propagates with light-like speed beyond optically excited depth. We further explored the possibility of forming an exciton–polariton quasiparticle due to abundant electron–hole pairs at $\mathbf{q}_{CDW}$. The electron and phonon heat diffusion cannot account for the propagation through the ~10 μm thickness. Moreover, ω_{AM} decreases with increasing fluence owing to a rise in the sample temperature, consistent with polarized Raman scattering measurements. Similar to previously reported ferroelectric materials [42,46], our results highlight the opportunity to engineer material response at an ultrafast time scale with external perturbations such as light.

Acknowledgments

R.R. and H.S. acknowledge the support from A. Sagdeo for XRD measurements of the polycrystalline sample. The simulations were performed at the SPACETIME-II super-computing facility at IITB and the ANUPAM super-computing facility at BARC. This research used resources of the Advanced Photon Source, a U.S. Department of Energy (DOE) Office of Science User Facility operated for the DOE Office of Science by Argonne National Laboratory under contract no. DE-AC02-06CH11357. Raman spectroscopy was performed at Raman laboratory at IIT Bombay. **Funding**: D.B. thanks the financial support from the Science & Engineering Research Board (SERB) under project no. CRG/2022/001317, BRNS–DAE under project no. 58/14/30/2019-BRNS/11117, and MoE/STARS under project no. MoE/STARS-1/345. **Author contributions**: R.R. and D.B.

conceived the idea and designed the experiments. R.R., H.S., D.B., and J.A.C. performed TXRD experiments and analyzed the data. V.D. and A.P.R. performed polarized Raman scattering experiments. M.K.G. and R.M. performed AIMD simulations. A.P. and A.B. performed electron and phonon heat diffusion simulations. R.K. and A.T. grew a single-crystal sample. R.R., D.B., and A.H.S. performed the IXS experiment. D.B. and R.R. wrote the first draft, and all authors commented on it. **Competing interests**: The authors declare that they have no competing interests.

Data Availability

Data that support the plots within this paper and other findings of this study are available from the corresponding authors upon reasonable request.

Supplementary Materials

Tables S1 to S5
Figs. S1 to S7

References

1. Gruner G. *Density waves in solids*. Reading (MA): Addison-Wesley; 1994.
2. Dressel M, Gruner G. *Electrodynamics of solids: Optical properties of electrons in matter*. Cambridge (UK): Cambridge University Press; 2002.
3. Johannes M, Mazin I. Fermi surface nesting and the origin of charge density waves in metals. *Phys Rev B*. 2008;77(16):165135.
4. Zhu X, Cao Y, Zhang J, Plummer E, Guo J. Classification of charge density waves based on their nature. *Proc Natl Acad Sci*. 2015;112(8):2367–2371.
5. Zhu X, Guo J, Zhang J, Plummer E. Misconceptions associated with the origin of charge density waves. *Adv Phys: X*. 2017;2(3):622–640.
6. Whangbo M-H, Canadell E, Foury P, Pouget J-P. Hidden fermi surface nesting and charge density wave instability in low-dimensional metals. *Science*. 1991;252(5002):96–98.
7. Roy AP, Bajaj N, Mittal R, Babu PD, Bansal D. Quasi-one-dimensional fermi surface nesting and hidden nesting enable multiple Kohn anomalies in α-uranium. *Phys Rev Lett*. 2021;126(9):096401.
8. Pathak A, Gupta MK, Mittal R, Bansal D. Orbital- and atom-dependent linear dispersion across the Fermi level induces charge density wave instability in $EuTe_4$. *Phys Rev B*. 2022;105(3):035120.
9. Rathore R, Pathak A, Gupta MK, Mittal R, Kulkarni R, Thamizhavel A, Singhal H, Said AH, Bansal D. Evolution of static charge density wave order, amplitude mode dynamics, and suppression of Kohn anomalies at the hysteretic transition in $EuTe_4$. *Phys Rev B*. 2023;107(2):024101.
10. Weber F, Rosenkranz S, Castellan JP, Osborn R, Hott R, Heid R, Bohnen KP, Egami T, Said AH, Reznik D. Extended phonon collapse and the origin of the charge-density wave in 2*H*-$NbSe_2$. *Phys Rev Lett*. 2011;107(10):107403.
11. Weber F, Hott R, Heid R, Bohnen KP, Rosenkranz S, Castellan JP, Osborn R, Said AH, Leu BM, Reznik D. Optical phonons and the soft mode in 2*H*-$NbSe_2$. *Phys Rev B*. 2013;87(24):245111.
12. Maschek M, Rosenkranz S, Heid R, Said AH, Giraldo-Gallo P, Fisher IR, Weber F. Wave-vector-dependent electron-phonon coupling and the charge-density wave transition in $TbTe_3$. *Phys Rev B*. 2015;91(23):235146.
13. Maschek M, Zocco DA, Rosenkranz S, Heid R, Said AH, Alatas A, Walmsley P, Fisher IR, Weber F. Competing soft phonon modes at the charge-density-wave transitions in $DyTe_3$. *Phys Rev B*. 2018;98(9):094304.
14. Chen C-W, Choe J, Morosan E. Charge density waves in strongly correlated electron systems. *Rep Prog Phys*. 2016;79(8):084505.
15. Gerber S, Jang H, Nojiri H, Matsuzawa S, Yasumura H, Bonn DA, Liang R, Hardy WN, Islam Z, Mehta A, et al. Three-dimensional charge density wave order in $YBa_2Cu_3O_{6.67}$ at high magnetic fields. *Science*. 2015;350(6263):949–952.
16. Boring A, Smith J. Plutonium condensed-matter physics: A survey of theory and experiment. *Los Alamos Sci*. 2000;26(1):90–127.
17. Söderlind P, Landa A, Sadigh B. Density-functional theory for plutonium. *Adv Phys*. 2019;68(1):1–47.
18. Kohn W. Image of the fermi surface in the vibration spectrum of a metal. *Phys Rev Lett*. 1959;2(9):393.
19. Zong A, Kogar A, Bie YQ, Rohwer T, Lee C, Baldini E, Ergeçen E, Yilmaz MB, Freelon B, Sie EJ, et al. Evidence for topological defects in a photoinduced phase transition. *Nat Phys*. 2019;15(1):27–31.
20. Lv B. Unconventional hysteretic transition in a charge density wave. *Physl Rev Lett*. 2022;128(3):036401.
21. Zhang C, Wu QY, Yuan YH, Zhang X, Liu H, Liu ZT, Zhang HY, Song JJ, Zhao YZ, Wu FY, et al. Angle-resolved photoemission spectroscopy study of the charge density wave order in layered semiconductor $EuTe_4$. *Phys Rev B*. 2022;106(20):L201108.
22. Zhang Q, Shi Y, Zhai KY, Zhao WX, Du X, Zhou JS, Gu X, Xu RZ, Li YD, Guo YF, et al. Thermal hysteretic behavior and negative magnetoresistance in an unusual charge-density-wave material $EuTe_4$. arXiv. 2023. https://doi.org/10.48550/arXiv.2303.02848
23. Kogar A, Zong A, Dolgirev PE, Shen X, Straquadine J, Bie YQ, Wang X, Rohwer T, Tung IC, Yang Y, et al. Light-induced charge density wave in $LaTe_3$. *Nat Phys*. 2020;16(2):159–163.
24. Gweon G-H, Denlinger JD, Clack JA, Allen JW, Olson CG, DiMasi E, Aronson MC, Foran B, Lee S. Direct observation of complete Fermi surface, imperfect nesting, and gap anisotropy in the high-temperature incommensurate charge-density-wave compound $SmTe_3$. *Phys Rev Lett*. 1998;81(4):886.
25. Brouet V, Yang WL, Zhou XJ, Hussain Z, Ru N, Shin KY, Fisher IR, Shen ZX. Fermi surface reconstruction in the CDW state of $CeTe_3$ observed by photoemission. *Phys Rev Lett*. 2004;93(12):126405.
26. Brouet V, Yang WL, Zhou XJ, Hussain Z, Moore RG, He R, Lu DH, Shen ZX, Laverock J, Dugdale SB, et al. Angle-resolved photoemission study of the evolution of band structure and charge density wave properties in RTe_3 (R= Y, La, Ce, Sm, Gd, Tb, and Dy). *Physl Rev B*. 2008;77(23):235104.
27. Garcia D, Gweon G-H, Zhou SY, Graf J, Jozwiak CM, Jung MH, Kwon YS, Lanzara A. Revealing charge density wave formation in the $LaTe_2$ system by angle resolved photoemission spectroscopy. *Phys Rev Lett*. 2007;98(16):166403.
28. Lee E, Kim DH, Denlinger JD, Kim J, Kim K, Min BI, Min BH, Kwon SY, Kang J-S. Angle-resolved and resonant photoemission spectroscopy study of the Fermi surface reconstruction in the charge density wave systems $CeTe_2$ and $PrTe_2$. *Phys Rev B*. 2015;91(12):125137.

29. Lee E, Kim DH, Kim HW, Denlinger JD, Kim H, Kim J, Kim K, Min BI, Min BH, Kwon YS, et al. The 7× 1 Fermi surface reconstruction in a two-dimensional *f*-electron charge density wave system: $PrTe_3$. *Sci Rep*. 2016;6(1):1–11.
30. Seong S, Lee E, Kwon YS, Min BI, Denlinger JD, Park B-G, Kang S-J. Angle-resolved photoemission spectroscopy study of rare-earth tritelluride charge density wave compounds: RTe_3 (*R*= Pr, Er). *Electron Struc*. 2021;3(2):024003.
31. Trigo M, Giraldo-Gallo P, Kozina ME, Henighan T, Jiang MP, Liu H, Clark JN, Chollet M, Glownia JM, Zhu D. Coherent order parameter dynamics in $SmTe_3$. *Phys Rev B*. 2019;99(10):104111.
32. Liu G, Ma X, He K, Li Q, Tan H, Liu Y, Xu J, Tang W, Watanabe K, Taniguchi T, et al. Observation of anomalous amplitude modes in the kagome metal CsV_3Sb_5. *Nat Commun*. 2022;13(1):1–8.
33. Nguyen QL, Duncan RA, Orenstein G, Huang Y, Krapivin V, de la Pena G, Ornelas-Skarin C, Reis DA, Abbamonte P, Bettler S. Ultrafast x-ray scattering from collective modes of the charge density wave in (TaSe4) $_2$I. arXiv. 2022. https://doi.org/10.48550/arXiv.2210.17483
34. Kim S, Lv Y, Sun XQ, Zhao C, Bielinski N, Murzabekova A, Qu K, Duncan RA, Nguyen QLD, Trigo M, et al. Observation of a massive phason in a charge-density-wave insulator. *Nat Mater*. 2023;22:429–433.
35. Sugai S, Takayanagi Y, Hayamizu N. Phason and amplitudon in the charge-density-wave phase of one-dimensional charge stripes in La_2–$x$$Sr_x$$Cu0_4$. *Phys Rev Lett*. 2006;96(13):137003.
36. Lavagnini M. Evidence for coupling between charge density waves and phonons in two-dimensional rare-earth tritellurides. *Phys Rev B*. 2008;78(20):201101.
37. Dolgirev PE, Rozhkov AV, Zong A, Kogar A, Gedik N, Fine BV. Amplitude dynamics of the charge density wave in $LaTe_3$: Theoretical description of pump-probe experiments. *Phys Rev Lett*. 2020;101(5):054203.
38. Huber T, Mariager SO, Ferrer A, Schäfer H, Johnson JA, Grübel S, Lübcke A, Huber L, Kubacka T, Dornes C, et al. Coherent structural dynamics of a prototypical charge-density-wave-to-metal transition. *Phys Rev Lett*. 2014;113(2):026401.
39. Yusupov R, Mertelj T, Chu J-H, Fisher I, Mihailovic D. Single-particle and collective mode couplings associated with 1-and 2-directional electronic ordering in metallic RTe−3 (R= Ho, Dy, Tb). *Phys Rev Lett*. 2008;101(24):246402.
40. Leuenberger D, Sobota JA, Yang S-L, Kemper AF, Giraldo-Gallo P, Moore RG, Fisher IR, Kirchmann PS, Devereaux TP, Shen Z-X. Classification of collective modes in a charge density wave by momentum-dependent modulation of the electronic band structure. *Phys Rev B*. 2015;91, no. 20:201106.
41. Singer A, Patel SKK, Kukreja R, Uhlir V, Wingert J, Festersen S, Zhu D, Glownia JM, Lemke HT, Nelson S, et al. Photoinduced enhancement of the charge density wave amplitude. *Phys Rev Lett*. 2016;117(5):056401.
42. Henstridge M, Först M, Rowe E, Fechner M, Cavalleri A. Nonlocal nonlinear phononics. *Nat Phys*. 2022;18(4):457–461.
43. Jin F, Itoh T, Goto T. Propagation velocity of exciton polariton in InI single crystals. *J Phys Soc Jpn*. 1989;58(7):2586–2596.
44. Bretscher HM, Andrich P, Murakami Y, Golež D, Remez B, Telang P, Singh A, Harnagea L, Cooper NR, Millis AJ, et al. Imaging the coherent propagation of collective modes in the excitonic insulator Ta_2NiSe_5 at room temperature. *Sci Adv*. 2021;7(28):eabd6147.
45. Feurer T, Vaughan JC, Nelson KA. Spatiotemporal coherent control of lattice vibrational waves. *Science*. 2003;299(5605):374–377.
46. Adachi S, Koehl RM, Nelson KA. Real-space and real-time imaging of polariton wavepackets. *J Lumin*. 2000;87:840–843.
47. Wang Y, Petrides I, McNamara G, Hosen MM, Lei S, Wu YC, Hart JL, Lv H, Yan J, Xiao D, et al. Axial Higgs mode detected by quantum pathway interference in RTe_3. *Nature*. 2022;1–6.
48. Wu D, Liu QM, Chen SL, Zhong GY, Su J, Shi LY, Tong L, Xu G, Gao P, Wang NL. Layered semiconductor $EuTe_4$ with charge density wave order in square tellurium sheets. *Phys Rev Mater*. 2019;3(2):024002.
49. Rathore R, Singhal H, Chakera J. Temporal evolution of photo-induced thermal strain in InSb probed by ultra-short laser produced Cu Kα x-rays. *J Appl Phys*. 2019;126(10):105706.
50. Toellner T, Alatas A, Said A. Six reflection meV-monochromator for synchrotron radiation. *J Synchrotron Radiat*. 2011;18:605–611.
51. Said A, Sinn H, Divan R. New developments in fabrication of high-energy-resolution analyzers for inelastic x-ray spectroscopy. *J Synchrotron Radiat*. 2011;18:492.
52. Said AH, Sinn H, Toellner TS, Alp EE, Gog T, Leu BM, Bean S, Alatas A. High-energy-resolution inelastic X-ray scattering spectrometer at beamline 30-ID of the advanced photon source. *J Synchrotron Radiat*. 2020;27(3):827–835.
53. Lovesey S. *Theory of neutron scattering from condensed matter*. Oxford: Clarendon Press; 1984.
54. Kresse G, Hafner J. Ab initio molecular dynamics for liquid metals. *Phys Rev B*. 1993;47:558.
55. Kresse G, Furthmuller J. Efficient iterative schemes for ab initio total-energy calculations using a plane-wave basis set. *Phys Rev B*. 1996;54:11169.
56. Kresse G, Furthmuller J. Efficiency of ab-initio total energy calculations for metals and semiconductors using a plane-wave basis set. *Comput Mater Sci*. 1996;6:15.
57. Shin K, Brouet V, Ru N, Shen Z, Fisher I. Electronic structure and charge-density wave formation in LaTe−1.95 and $CeTe_{2.00}$. *Phys Rev B*. 2005;72(8):085132.
58. Malliakas C, Billinge SJ, Kim HJ, Kanatzidis MG. Square nets of tellurium: Rare-earth dependent variation in the charge-density wave of RETe−3 (RE= rare-earth element). *J Am Chem Soc*. 2005;127(18):6510–6511.
59. Ru N, Condron CL, Margulis GY, Shin KY, Laverock J, Dugdale SB, Toney MF, Fisher IR. Effect of chemical pressure on the charge density wave transition in rare-earth tritellurides RTe_3. *Phys Rev B*. 2008;77(3):035114.
60. Block A, Liebel M, Yu R, Spector M, Sivan Y, García de Abajo FJ, van Hulst NF. Tracking ultrafast hot-electron diffusion in space and time by ultrafast thermomodulation microscopy. *Sci Adv*. 2019;5(5):eaav8965.
61. Pathak A, Pawnday A, Roy AP, Aref AJ, Dargush GF, Bansal D. MCBTE: A variance-reduced Monte Carlo solution of the linearized Boltzmann transport equation for phonons. *Comput Phys Commun*. 2021;265:108003.
62. Tritt T. *Thermal conductivity: Theory, properties, and applications*. New York: Kluwer Academic/Plenum Publishers; 2004.
63. Klemens P. *Solid state physics: Advances in research and applications—Thermal conductivity and lattice vibrational modes*. New York: Academic Press Inc.; 1958.
64. Cavalleri A, Siders CW, Brown FLH, Leitner DM, Tóth C, Squier JA, Barty CPJ, Wilson KR, Sokolowski-Tinten K, Horn von Hoegen M, et al. Anharmonic lattice dynamics in

germanium measured with ultrafast X-ray diffraction. *Phys Rev Lett*. 2000;85(3):586.
65. Wingert J, Singer A, Patel SKK, Kukreja R, Verstraete MJ, Romero AH, Uhlir V, Festersen S, Zhu D, Glownia JM, et al. Direct time-domain determination of electron-phonon coupling strengths in chromium. *Phys Rev B*. 2020;102(4):041101.
66. Taboada-Gutiérrez J, Álvarez-Pérez G, Duan J, Ma W, Crowley K, Prieto I, Bylinkin A, Autore M, Volkova H, Kimura K, et al. Broad spectral tuning of ultra-low-loss polaritons in a van der Waals crystal by intercalation. *Nat Mater*. 2020;19(9):964–968.
67. Wu Y, Ou Q, Yin Y, Li Y, Ma W, Yu W, Liu G, Cui X, Bao X, Duan J, et al. Chemical switching of low-loss phonon polaritons in α-MoO_3 by hydrogen intercalation. *Nat Commun*. 2020;11(1):1–8.
68. Pavlidis G, Schwartz JJ, Matson J, Folland T, Liu S, Edgar JH, Caldwell JD, Centrone A. Experimental confirmation of long hyperbolic polariton lifetimes in monoisotopic (10B) hexagonal boron nitride at room temperature. *APL Mater*. 2021;9(9):091109.
69. Ni G, McLeod AS, Sun Z, Matson JR, Lo CFB, Rhodes DA, Ruta FL, Moore SL, Vitalone RA, Cusco R, et al. Long-lived phonon polaritons in hyperbolic materials. *Nano Lett*. 2021;21(13):5767–5773.
70. Su R, Wang J, Zhao J, Xing J, Zhao W, Diederichs C, Liew TCH, Xiong Q. Room temperature long-range coherent exciton polariton condensate flow in lead halide perovskites. *Sci Adv*. 2018;4(10):eaau0244.
71. Ikehara T, Itoh T. Dynamical behavior of the exciton polariton in CuCl: Coherent propagation and momentum relaxation. *Phys Rev B*. 1991;44(17):9283.
72. Pandya R, Ashoka A, Georgiou K, Sung J, Jayaprakash R, Renken S, Gai L, Shen Z, Rao A, Musser AJ. Tuning the coherent propagation of organic exciton-polaritons through dark state delocalization. *Adv Sci (Weihn)*. 2022;2105569.